Monthly Notices
of the
ROYAL ASTRONOMICAL SOCIETY

Mon. Not. R. Astron. Soc. **400,** 791–804 (2009) doi:10.1111/j.1365-2966.2009.15479.x

Chemical evolution of high-mass stars in close binaries – II. The evolved component of the eclipsing binary V380 Cygni

K. Pavlovski,[1⋆] E. Tamajo,[1] P. Koubský,[2] J. Southworth,[3] S. Yang[4] and V. Kolbas[1]

[1]*Department of Physics, University of Zagreb, Bijenička cesta 32, 10000 Zagreb, Croatia*
[2]*Astronomical Institute of the Academy of Sciences, 251 65 Ondřejov, Czech Republic*
[3]*Department of Physics, University of Warwick, Coventry CV4 7AL*
[4]*Department of Physics and Astronomy, University of Victoria, Victoria, BC V8W3P6, Canada*

Accepted 2009 August 2. Received 2009 July 25; in original form 2009 June 4

ABSTRACT

The eclipsing and double-lined spectroscopic binary V380 Cyg is an extremely important probe of stellar evolution: its primary component is a high-mass star at the brink of leaving the main sequence whereas the secondary star is still in the early part of its main sequence lifetime. We present extensive high-resolution échelle and grating spectroscopy from Ondřejov, Calar Alto, Victoria and La Palma. We apply spectral disentangling to unveil the individual spectra of the two stars and obtain new spectroscopic elements. The secondary star contributes only about 6 per cent of the total light, which remains the main limitation to measuring the system's characteristics. We determine improved physical properties, finding masses 13.1 ± 0.3 and $7.8 \pm 0.1\,M_{\odot}$, radii 16.2 ± 0.3 and $4.06 \pm 0.08\,R_{\odot}$, and effective temperatures $21\,750 \pm 280$ and $21\,600 \pm 550$ K, for the primary and secondary components, respectively. We perform a detailed abundance analysis by fitting non-local thermodynamic equilibrium (LTE) theoretical line profiles to the disentangled spectrum of the evolved primary star, and reveal an elemental abundance pattern reminiscent of a typical nearby B star. Contrary to the predictions of recent theoretical evolution models with rotational mixing, no trace of abundance modifications due to the CNO cycle are detected. No match can be found between the predictions of these models and the properties of the primary star: a mass discrepancy of $1.5\,M_{\odot}$ exists and remains unexplained.

Key words: binaries: eclipsing – stars: fundamental parameters.

1 INTRODUCTION

The last decade has witnessed a huge improvement in modelling the structure and evolution of stars, particularly for higher masses. The inclusion of effects such as rotation and/or magnetic fields has caused substantial changes in the resulting predictions (see Maeder & Meynet 2000; Langer et al. 2008). Some of these concern evolutionary changes in the chemical composition of stellar atmospheres. Due to the CNO cycle in the core of high-mass stars some elements are enhanced, such as helium and nitrogen, and some are depleted, like carbon and to a lesser extent oxygen. With deep mixing due to rotation, the products of core nucleosynthesis are predicted to be brought to the stellar surface and cause changes in atmospheric abundance patterns. Rotational mixing is so efficient that changes in the atmospheric composition should be identifiable whilst the star is still on the main sequence (MS).

Anomalous abundances of helium and CNO elements have been noted for many years (Leushin 1988; Lyubimkov 1998), and confirmed in detail by Gies & Lambert (1992), and more recently for helium abundances in B stars by Lyubimkov, Rostopchin & Lambert (2004, hereafter LRL04) and Huang & Gies (2006). However, more ambitious observational studies indicate that the situation is not straightforward. In a survey of OB stars in our Galaxy and the Magellanic Clouds, multi-object spectroscopy for about 750 stars were secured by Evans et al. (2005, 2006). Elemental abundances were separately determined for both slow (Hunter et al. 2007; Trundle et al. 2007) and fast (Hunter et al. 2008, 2009) rotators in the Large Magellanic Cloud. Since theoretical calculations predict the strongest effect to be the enhancement of the nitrogen abundance (about 0.5 dex up to the terminal age of the MS, TAMS), Hunter et al. (2008) examined the abundances of this element in detail. They found a rather complex behaviour: nitrogen enrichment is correlated with projected rotational velocity, but there are some slow rotators with a high nitrogen abundance. Their findings corroborate a recent study by Morel et al. (2006), who analysed a sample of slowly rotating Galactic β Cephei stars and found a group with nitrogen enrichment. Importantly, Morel et al. (2006) were able to link this with enhanced magnetic field strengths. It is clear that several physical phenomena and processes affect the

⋆E-mail: pavlovski@phy.hr

surface chemical compositions of high-mass stars, and it is a challenge to disentangle them.

Empirical constraints on these processes remain hard to come by, despite a steady improvement in observational techniques and capabilities (see Hilditch 2004). In this series of papers, we aim to calibrate the abundance patterns and chemical evolution of high-mass stars by analysing detached eclipsing binaries (dEBs). These are vital for specifying empirical constraints on the properties of high-mass stars, since they are the primary source of directly measured stellar properties (Andersen 1991). Unfortunately, accurate (2 per cent or better) physical properties are available for only 10 dEBs containing $> 10\,M_\odot$ stars,[1] and only four have observational constraints on their chemical composition. Chemical abundances are difficult to determine for high-mass dEBs for several reasons. First, they tend to display only a small number of spectral lines. Secondly, their often high rotational velocities means the lines are wide and shallow. Thirdly, in dEBs the spectral lines from the two components interfere with each other ('line blending').

In a seminal work, Simon & Sturm (1994) introduced the technique of *spectral disentangling* (SPD), by which *individual* spectra of the component stars of double-lined spectroscopic binary systems can be deduced from observations covering a range of orbital phases. SPD can be used to measure spectroscopic orbits which are not affected by line blending (see Southworth & Clausen 2007). The resulting disentangled spectra also have a much higher S/N than the original observations, so are well suited to chemical abundance analyses. As a bonus, the strong degeneracy between effective temperature ($T_{\rm eff}$) and surface gravity ($\log g$) is not a problem for dEBs because surface gravities can be measured directly and to high accuracy (0.01 dex or better). A detailed investigation of these possibilities is given by Pavlovski & Hensberge (2005, hereafter PH05).

1.1 The eclipsing binary system V380 Cygni

V380 Cyg is a very interesting probe of stellar structure and evolution because it contains a primary (star A) which is rather evolved ($\log g = 3.1$) and a less massive secondary (star B) which is not ($\log g = 4.1$). A thorough study by Popper & Guinan (1998) and Guinan et al. (2000, hereafter G2000) disclosed that star A is the more luminous and massive component of the system, lying near the 'blue hook' of the MS, and that star B is a $\sim$3 mag fainter evolve MS star. Due to the faintness of star B, V380 Cyg was categorized as a single-lined spectroscopic binary for many years (Batten 1962, and references therein). Hill & Batten (1984) applied cross-correlation techniques to considerably improve the orbital elements. Further advances were possible only by high-resolution and high signal-to-noise (S/N) spectroscopy (Lyubimkov et al. 1996; Popper & Guinan 1998).

The eclipses in V380 Cyg are rather shallow (amplitudes of 0.12 and 0.09 mag) and occur on an orbital period of 12.4 d. The radii of the stars are not determined to high accuracy despite considerable effort spent on securing a precise and complete light curve (G2000). These difficulties have contributed to disagreements over which of the two stars is hotter (Hill & Batten 1984; Lyubimkov et al. 1996; G2000). The best estimate of $T_{\rm eff\ A}$ to date came from fitting ultraviolet and visual spectrophotometry with model atmosphere energy distributions, giving $T_{\rm eff} = 21\,350$ K (G2000). There is also a discrepancy in the derived masses of the components. The two most recent studies give $M_{\rm A} = 11.1 \pm 0.5\,M_\odot$ and $M_{\rm B} = 6.95 \pm 0.25\,M_\odot$ (G2000) and $M_{\rm A} = 12.1 \pm 0.3\,M_\odot$ and $M_{\rm B} = 7.3 \pm 0.3\,M_\odot$ (Lyubimkov et al. 1996).

V380 Cyg has an eccentric orbit and displays the phenomenon of apsidal motion with a rate of $\dot\omega = 24\overset{\circ}{.}0 \pm 1\overset{\circ}{.}8$ per 100 yr (G2000). To match the observed stellar properties to theoretical evolutionary tracks these authors found that a large core-overshooting parameter is required, $\alpha_{\rm ov} = 0.6 \pm 0.1$. In the Hertzsprung–Russell (HR) diagram, star A is predicted to be located near the blue point of the MS hook. G2000 drew a general conclusion that high-mass stars have large convective cores, so are more centrally condensed than predicted by standard evolutionary theory. However, theoretical work by Claret (2003, 2007) does not corroborate this conclusion, finding instead that $\alpha_{\rm ov} = 0.4^{+0.2}_{-0.3}$ for this dEB.

The chemical composition of V380 Cyg, in particular the helium abundances, was studied by Leushin & Topilskaya (1986) and Lyubimkov et al. (1996). Both groups found star A to be enriched in helium and star B to be normal. A major goal of our work is to improve and extend these results, and thus be able to perform a detailed comparison with theoretical stellar models.

2 SPECTROSCOPIC DATA

Star B is barely visible in the optical spectrum of the binary – G2000 estimated the light ratio in the visual band to be $L_{\rm A}/L_{\rm B} \sim 14.5$. A successful observational programme therefore requires high-resolution and high-S/N spectroscopy. For this study, we have secured spectra at four different observatories, using either diffraction grating or échelle spectrographs. Observing logs are given in the Appendix (available in the electronic version of this work).

2.1 Ondřejov spectra

59 spectra of V380 Cyg were obtained at the Astronomical Institute of the Academy of Sciences of the Czech Republic in Ondřejov. The observations were made in 2004–2007 with the 2-m telescope and the coudé spectrograph. The spectral interval centred on the Hα line covers about 500 Å at a dispersion of 17 Å mm^{-1}, whilst the spectral intervals centred on the Hβ and Hγ lines cover around 250 Å, at a dispersion 8.5 Å mm^{-1}.

2.2 Calar Alto spectra

We obtained 43 spectra of V380 Cyg in the course of two observing runs (2008 May and August) at the Centro Astronómico Hispano Alemán (CAHA) at Calar Alto, Spain. We used the 2.2-m telescope, FOCES échelle spectrograph (Pfeiffer et al. 1998), and a Loral #11i CCD binned 2×2 to decrease the readout time. With a grating angle of 2724, prism angle of 130 and a 150 μm slit, we obtained a spectral coverage of roughly 3700–9200 Å in each exposure, at a resolving power of $R \approx 40\,000$. Wavelength calibration was performed using thorium–argon exposures, and flat-fields were obtained using a tungsten lamp. The observing conditions were generally good but several exposures were affected by clouds.

2.3 Victoria spectra

Spectra were obtained with the 1.2-m McKellar telescope and its coudé spectrograph at Dominion Astrophysical Observatory (DAO) with a dispersion of 9 Å mm^{-1}. A total of 27 spectra were secured in the region of the Hα line ($\lambda\lambda$6150–6760), mostly in the years

[1] An up-to-date compilation of the properties of well-studied dEBs is maintained at http://www.astro.keele.ac.uk/∼jkt.

1996–2000. In the present work, we have used only the five spectra secured in 2006–2007, as the orbital parameters gradually change due to apsidal motion.

2.4 La Palma spectra

15 spectra of V380 Cyg were obtained in 2006 November with the Nordic Optical Telescope (NOT) and FIES échelle spectrograph (Frandsen & Lindberg 1999) at La Palma. We used the medium-resolution fibre which yielded a resolving power of $R = 47\,000$ and a fixed wavelength coverage of 3640–7360 Å. Wavelength calibration was performed using thorium–argon exposures, and flat-fields were obtained using a halogen lamp. The observing conditions were generally reasonable (for winter in La Palma) but several exposures suffered from thin cloud coverage or poor seeing.

2.5 Data reduction

The échelle spectra (from CAHA and NOT) were bias subtracted, flat-fielded and extracted with the IRAF[2] échelle package routines. Normalization and merging of the orders were performed with great care, using programs developed by us, to ensure that these steps did not cause any systematic errors in the resulting spectra.

The Ondřejov spectra were reduced by the program SPEFO (Horn et al. 1996; Škoda 1996). Initial reduction of the DAO spectra (bias subtraction, flat-fielding and spectrum extraction) were carried out in IRAF. The wavelength calibrations were based on thorium–argon lamp spectra, and were performed by using SPEFO.

3 METHOD

Our analysis follows the methods introduced by Hensberge, Pavlovski & Verschueren (2000) and PH05 in their studies of the eclipsing and double-lined spectroscopic binary V578 Mon, and elaborated in Pavlovski & Southworth (2009, hereafter Paper I). The core of this approach is the reconstruction of individual stellar spectra from the observed composite spectra using SPD, which allows a detailed abundance analysis using the same tools as for single stars (cf. Pavlovski 2004; Hensberge & Pavlovski 2007). SPD also gives the velocity amplitudes of the two stars which, in combination with modelling of V380 Cyg's light curves, yields the physical properties of the two stars including precise and accurate surface gravity measurements which are vital for the abundance analyses.

The method of SPD returns the individual spectra of the two components of a binary star, but their normalization is arbitrary. This is because the continuum light ratio of the two stars is *not* directly measurable from composite spectra, short of ensuring individual spectral lines do not dip below zero flux. Whilst relative line strengths in a spectrum are reliable, their absolute scaling must be recovered from elsewhere. Here, we have renormalized our disentangled spectra using the stellar light ratios found in the light-curve analysis (Section 5), following the procedure described in detail by PH05, and taking into account the line-blocking inherent to the Fourier disentangling method.

We have estimated chemical abundances by fitting the renormalized disentangled spectra with synthetic spectra. Non-LTE line formation and spectrum synthesis computations were performed using DETAIL and SURFACE (Giddings 1981; Butler 1984) and the model atoms as listed in Paper I. Model atmospheres were calculated with ATLAS9 (Kurucz 1979). Justification for this hybrid approach can be found in Nieva & Przybilla (2007).

SPD can be quite sensitive to the precise phase distribution and continuum normalization of the observed composite spectra. Hynes & Maxted (1998) have shown that this is not a problem for radial velocity studies, where Hensberge, Ilijić & Torres (2008) have demonstrated that it is important for correct reproduction of the overall shape of disentangled spectra. A lack of significant time variability in the relative light contributions of the two star can produce spurious patterns in separated spectra, which in practise appear as typically low-frequency continuum variations. Hensberge et al. (2008) examined this in detail and found that the phenomenon arises due to degeneracy of the SPD equations and/or bias progression from the observed spectra. Careful planning of an observing run and the subsequent data reduction and analysis can mostly overcome these difficulties, in particular by observing the target during eclipses. In the case of V380 Cyg, we were hampered by the relative faintness of the secondary star, but were able to secure spectra with a very good distribution in orbital phase. Combined with a careful data reduction (particularly concerning continuum normalization and échelle order merging), this approach has allowed us to obtain high-quality disentangled spectra which can be used for abundance analysis.

4 SPECTROSCOPIC ORBITS THROUGH SPECTRAL DISENTANGLING

In the method of SPD as introduced by Simon & Sturm (1994), one solves both for the individual spectra of the components, and the optimal set of orbital parameters. Here, we have performed a SPD analysis in the Fourier space as formulated by Hadrava (1995), which has one big advantage. The system of equations consists of $N_{\rm obs} \times N_{\rm pix}$ coupled equations linear in a little more than $2N_{\rm pix}$, where $N_{\rm obs}$ is the number of observed spectra, and $N_{\rm pix}$ is the number of data points per observed spectrum. Using discrete Fourier transforms, this large system of equations can be coupled into $(N_{\rm pix}/2) + 1$ systems of $N_{\rm obs}$ complex equations involving only two unknowns in the case of binary systems, and the required computation time is significantly smaller. In this work, we have performed SPD on a large spectral range about 3000 Å wide, for which the speed advantage of Fourier disentangling is very important. The disadvantage is that weights can be assigned only to whole spectra, and not to individual pixels. We weighted the spectra according to S/N. We use the FDBINARY[3] code described by Ilijić et al. (2004).

SPD was performed in spectral regions centred on the prominent He I lines. The contribution of star B to the total system light is rather small ($L_{\rm A}/L_{\rm B} \sim 15.5$ in V), and its lines are difficult to see. Fortunately, star B has a similar $T_{\rm eff}$ to star A (Section 6), and so is best seen in the He I lines. Star B's lines also emerge in other regions of its disentangled spectrum, but are very weak so are of limited use for determining orbital elements. We therefore concentrated only on the stronger helium lines. After some trial calculations, we selected six spectral regions centred on the lines at λλ 4026, 4388, 4471 (including Mg II λ4481), 4712, 4912 and 6670 Å for measuring the orbital elements. We also grouped the spectra into appropriate time intervals to account for the change in ω due to apsidal motion (amounting to about 6° between our first and last spectrum). Table 1 lists the final orbital elements, which are the mean and rms of the values derived from all spectral regions.

[2] IRAF is distributed by the National Optical Astronomy Observatory, which is operated by the Association of the Universities for Research in Astronomy, Inc., under cooperative agreement with the NSF.

[3] http://sail.zpf.fer.hr/fdbinary/

Table 1. Parameters of the spectroscopic orbits for V380 Cyg derived in this work. Throughout the SPD analysis, the period was kept fixed to the value derived by G2000.

Orbital period (d)	12.425719 (fixed)
Time of periastron passage (HJD)	2454615.18 ± 0.14
Velocity amplitude K_A (km s^{-1})	95.1 ± 0.3
Velocity amplitude K_B (km s^{-1})	160.5 ± 1.2
Mass ratio q	0.592 ± 0.005
Orbital eccentricity e	0.206 ± 0.008
Longitude of periastron ω (°)	134.2 ± 1.1

How does our solution compare to previous results? Batten (1962) made a comprehensive study of all available photographic spectra, and measured the lines of star B for the first time. He found $K_A = 93.4 \pm 2.0\,\mathrm{km\,s^{-1}}$ and $K_B = 160.9 \pm 2.9\,\mathrm{km\,s^{-1}}$, which are very close to our values. Hill & Batten (1984) studied existing and new photographic spectra, and found a discrepancy between the systemic velocities of the two stars. Their K_B is about 7 km s^{-1} larger than that of Batten, which increases the mass of star A from 12.5 to 13.7 $M_\odot$. Lyubimkov et al. (1996) collected all available RV measurements for V380 Cyg, including new CCD observation. They found a much smaller K_B of 155.3 km s^{-1} and a slightly larger K_A of 93.95 km s^{-1}, but gave no uncertainties. The most comprehensive investigation to date is that of Popper & Guinan (1998), based on high resolution and high-S/N échelle spectra. They adopted the average of their own and Lyubimkov's solutions, arriving at $K_A = 95.6 \pm 0.5\,\mathrm{km\,s^{-1}}$ and $K_B = 151 \pm 3\,\mathrm{km\,s^{-1}}$. Our own results compare well for K_A, but a discrepancy of 10 km s^{-1} exists for K_B.

The main source of error in RV measurement by cross-correlation is the selection of the template spectrum. SPD bypasses this problem entirely by directly seeking the best overall solution for both the spectra and the orbital elements. Therefore, it does not require guidance from a template spectrum or pass through an intermediate step of obtaining RV measurements from each observed spectrum. An additional advantage of this approach is that it is not biased by line blending. Unfortunately, a dedicated study of error propagation in SPD is still lacking, and the best we can do is split our spectra into different sets and different wavelength regions to obtain several independent measurements of the orbital parameters (Table 1). Recently, Southworth & Clausen (2007) have performed an extensive analysis of orbits derived by double Gaussian fitting, cross-correlation and SPD. The SPD orbits were the most internally consistent, followed by double Gaussian fitting. The cross-correlation results were affected by line blending, even after attempts were made to correct for this. Southworth & Clausen (2007) noted that their SPD solutions had several local minima around the best fit, and used a grid search to deal with this.

We therefore ascribe the 10 km s^{-1} discrepancy in K_B to line blending in the cross-correlation solutions. Our K_B was found by SPD, which does not suffer from line blending or template errors, and should be preferred. Finally, as line blending is not a problem for SPD, we could use all of our spectra rather than just those where the lines of the two stars are resolved. Disentangled profiles of the He I λ4471 and Mg II λ4481 lines are shown in Fig. 1.

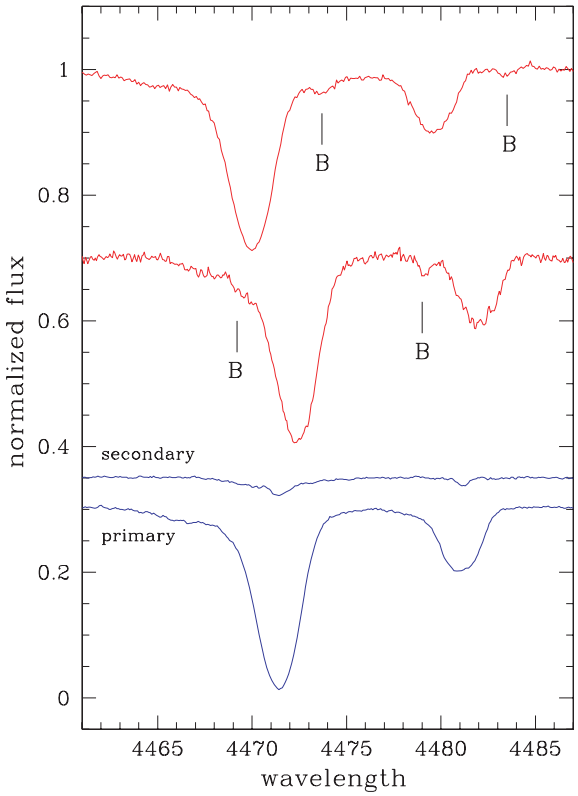

Figure 1. Observed spectra around the He I λ4471 and Mg II λ4481 lines. The upper two spectra were obtained near quadrature, and weak lines of the secondary are visible and indicated with 'B'. The lower two spectra are disentangled spectra of the components. The faintness of star B compared to star A is obvious.

5 LIGHT-CURVE ANALYSIS

Driven by suspicions that the secondary star of V380 Cyg might be hotter than the primary star (see below), we have revisited the light curves presented by G2000. These data were obtained using the Automated Photometric Telescopes at Mt. Hopkins, Arizona, and total 870 observations in the *UBV* bandpasses.

The light curves show substantial ellipsoidal modulation and reflection effect, so we have used the Wilson–Devinney (WD) code (Wilson & Devinney 1971; Wilson 1979, 1993), which implements Roche geometry and a detailed treatment of reflection and other physical phenomena, version of 2004 February 06. We have modified WD to automatically converge to the best solution using either a damped version of the standard differential corrections procedure (DC) or the robust downhill simplex algorithm AMOEBA (Press et al. 1992). For our final solutions, we used DC and iterated until all parameter corrections were less than half of their formal errors.

The full set of fixed and control parameters are given in Table 2: for our modelling, we adopted the orbital ephemeris from G2000, bolometric albedos and gravity brightening exponents appropriate for radiative atmospheres (Claret 1998, 2001) and pseudo-synchronous rotation for both stars. Using the detailed reflection technique of Wilson (1990) did not substantially improve the fit and much increased the calculation time, so was not used.

The treatment of limb darkening can be important, and there is evidence that theoretically predicted coefficients are imperfect (Southworth 2008; Southworth et al. 2009). We therefore included limb darkening in three different ways: using coefficients obtained by bilinear interpolation in the tables of Van Hamme (1993) or Claret (2000) or including the coefficients as fitted parameters. The solutions show a negligible dependence on the way limb darkening is accounted for, probably because the eclipses are quite shallow

Table 2. Summary of the fixed and control parameters for our final WD solutions of the G2000 light curves of V380 Cyg. For further details, please see the WD user guide (Wilson & Van Hamme 2004).

Parameter	WD name	Star A	Star B
Orbital period (d)	PERIOD	12.425719	
Reference time (HJD)	HJD0	2441256.544	
Mass ratio	RM	0.5916	
Stellar $T_{\rm eff}$s (K)	TAVH, TAVC	21 500	22 000
Rotation rates	F1, F2	1.0	1.0
Stellar albedos	ALB1, ALB2	1.0	1.0
Gravity darkening	GR1, GR2	1.0	1.0
Numerical accuracy	N1, N2	60	30
Bolometric LD coefficient	XBOL1, XBOL2	0.6475	0.6854
U LD coefficient	X1, Y1	0.3582	0.3128
B LD coefficient	X1, Y1	0.3534	0.3026
V LD coefficient	X1, Y1	0.3043	0.2622

compared to the observational scatter. For our final solutions, we used the linear limb darkening law and fixed the coefficients at the Van Hamme (1993) values (Table 2).

5.1 The effective temperatures

The light curves of dEBs contain almost no information about the absolute $T_{\rm eff}$s of the component stars: only the *ratio* of the $T_{\rm eff}$s is directly derivable from normal light curves. One of our goals was to investigate the quality of solutions where star B was hotter than star A. For one set of solutions, we therefore fixed $T_{\rm eff\ A} = 21\,500$ K and then fixed $T_{\rm eff\ B}$ to values between 18 000 and 25 000 K in steps of 250 K. The best fit was found for each $T_{\rm eff\ B}$, and for the three light curves both individually and in combination. Fig. 2 is a plot of the quality of the fits for these solutions, and shows a preference for solutions with $T_{\rm eff B} > T_{\rm eff A}$.

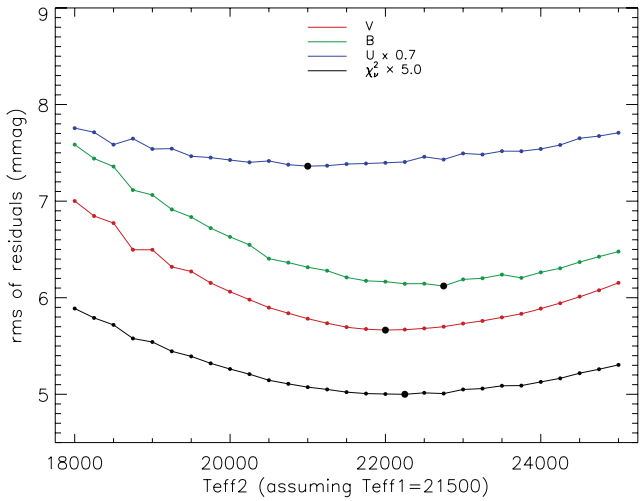

Figure 2. Quality of the solutions for the *UBV* light curves individually and in combination, for $T_{\rm eff\ A} = 21\,500$ K and $T_{\rm eff\ B}$ fixed at a range of values. For the individual light curves, the solution quality is given by the rms of the residuals, and for the combined solution the reduced χ^2 assuming observational errors equal to the rms value for each light curve. The points at which a fit was evaluated or the best fit was found is given by small and large filled circles, respectively.

5.2 Final light-curve solutions

We have obtained final solutions for the *UBV* light curves both individually and in combination, using our damped version of DC to optimize the fits. WD allows the use of predictions from Kurucz (1993) model atmospheres to link the flux ratios in different passbands, which means the results have a dependence on theoretical models. We prefer to avoid this option (MODE = 0 and IPB = 1; Wilson & Van Hamme 2004), particularly as the available data are multiband and include the very blue *U* passband. We therefore fit for the light contribution of each star in each passband independently, after assuming reasonable $T_{\rm eff}$s with which the limb darkening coefficients are derived.

We fixed $T_{\rm eff\,A} = 21\,500$ K and $T_{\rm eff\,B} = 22\,000$ K, and then fitted for the potentials of the two stars, the orbital inclination, eccentricity and periastron longitude, a phase shift, and the light contributions of the two stars in each passband. Additional light from a third star was not considered (see G2000).

The three light curves were fitted together to give the final parameter values, and then individually to check for consistency. In Table 3, we report the fitted parameters and their formal errors (calculated by DC from the covariance matrix), and in Fig. 3 we show the fits to the data. The volume-equivalent fractional radii of the two stars were obtained using the WD LC program.

We caution that the formal errors can be optimistic when there are strong correlations between parameters, so should be considered with care. Taking the formal errors at face value indicates poor agreement between light curves, with reduced χ^2 values of 4.2 and 3.4 for the stellar potentials, 3.4 for the inclination and a huge 96.9 and 19.7 for e and ω. This highlights the limitations of formal errors, as e and ω are strongly correlated in situations such as this one (e.g. Southworth, Maxted & Smalley 2004; Southworth, Bruntt & Buzasi 2007). For our final light-curve parameters, we instead adopt the values from the combined fit to the three light curves and the uncertainties from the scatter between the separate solutions for these light curves.

6 SPECTRAL ANALYSIS OF BOTH COMPONENTS

A model atmosphere is defined to first order by its $T_{\rm eff}$ and $\log g$, and when fitting observational data these two parameters can be quite correlated. This can be a major limitation for abundance analyses of single stars, but in the case of dEBs it is possible to accurately measure their $\log g$s from light and velocity curve analysis. In the case of V380 Cyg, we have measured $\log g_{\rm A} = 3.136 \pm 0.014$ and $\log g_{\rm B} = 4.112 \pm 0.017$ (Section 7).

6.1 Effective temperature determination

The $T_{\rm eff}$s of B stars are best determined from the silicon ionization balance (Becker & Butler 1990). Lines of Si II and Si III are present in the disentangled spectrum of V380 Cyg A – the lack of Si IV lines indicates that $T_{\rm eff\,A} < 24\,000$ K. Grids of synthetic spectra were calculated for $T_{\rm eff} = 19\,000$–$24\,000$ K and for $\log g = 3.136$. Equivalent widths (EWs) were measured in IRAF for the Si II ($\lambda\lambda$ 4128, 4130, 5031) and Si III ($\lambda\lambda$ 4552, 4567, 5039) lines, and calibration curves produced for Si II/Si III EW ratios. EW measurements were made for star A and a mean value of $T_{\rm eff\,A} = 21\,750 \pm 220$ K was found from six EW ratios. Absolute EWs can only be measured from disentangled spectra once they have been carefully renormalized, but the *ratios* of EWs are reliable.

Table 3. Results of the WD code modelling process of the G2000 light curves of V380 Cyg. For the final column, the uncertainties come from the scatter of the individual solutions for the U, B and V data. For the other columns, the uncertainties are formal errors calculated by the WDDC code.

Parameter	WD name	U	B	V	Combined	Adopted
Star A potential	PHSV	4.698 ± 0.073	4.541 ± 0.030	4.587 ± 0.039	4.609 ± 0.029	4.609 ± 0.046
Star B potential	PCSV	10.75 ± 0.25	10.51 ± 0.14	10.26 ± 0.14	10.51 ± 0.12	10.51 ± 0.17
Orbital inclination (°)	XINCL	80.76 ± 0.58	80.63 ± 0.17	81.25 ± 0.31	81.01 ± 0.21	81.01 ± 0.27
Orbital eccentricity	E	0.2207± 0.0042	0.2023± 0.0021	0.1831± 0.0017	0.1979± 0.0017	0.198 ± 0.012
Periastron longitude (°)	PERR0	136.5 ± 2.7	140.3 ± 1.7	150.1 ± 2.1	143.2 ± 1.5	143.2 ± 5.3
Phase shift	PSHIFT	−0.0459± 0.0009	−0.0460± 0.0004	−0.0480± 0.0004	−0.0470± 0.0004	
U-band light from star A	HLUM	12.008 ± 0.046			12.055 ± 0.027	12.055
U-band light from star B	CLUM	0.734 ± 0.045			0.697 ± 0.026	0.697
B-band light from star A	HLUM		9.443 ± 0.023		9.447 ± 0.025	9.447
B-band light from star B	CLUM		0.618 ± 0.022		0.611 ± 0.024	0.611
V-band light from star A	HLUM			9.823 ± 0.024	9.805 ± 0.025	9.805
V-band light from star B	CLUM			0.619 ± 0.023	0.635 ± 0.025	0.635
Fractional radius of star A		0.2563	0.2660	0.2615	0.2609	0.2609 ± 0.0040
Fractional radius of star B		0.06391	0.06538	0.06701	0.06534	0.0653 ± 0.0013
U-band rms of residuals (mmag)		10.386			10.524	
B-band rms of residuals (mmag)			5.964		6.130	
V-band rms of residuals (mmag)				5.782	5.635	

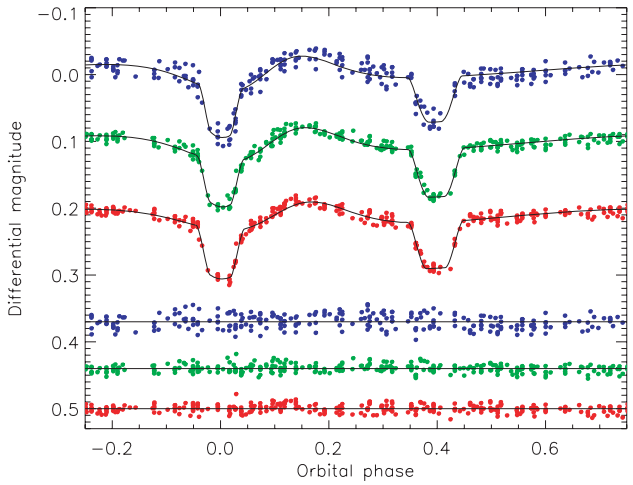

Figure 3. Comparison between the best fits found with the WD code and the light curves presented by G2000. The residuals are shown at the base of the plot with offsets from zero. In each case, the top (blue) data are U, the middle (green) are B and the lower (red) are V.

A second way of measuring $T_{\rm eff}$s of B stars is to study the shape of the hydrogen Balmer lines. The usual degeneracy between $T_{\rm eff}$ and $\log g$ is not a problem here, as the $\log g$ values of the stars are known, but this method does require a careful renormalization of the disentangled spectra. We used light factors derived from the light-curve analysis (Section 5), whose variation with wavelength is small in the region covered by Hδ, Hγ and Hβ. We avoid Hα, since it is formed high in the stellar atmosphere and is not a good $T_{\rm eff}$ indicator. The fitting was done with a routine for multiparameter optimization, which uses a genetic algorithm to minimize χ^2 (Tamajo, Pavlovski & Southworth 2009). The projected rotational velocity was fixed to $v \sin i = 98\,{\rm km\,s^{-1}}$ (Section 6.2). Runs were performed in which just $T_{\rm eff}$ (run 1) or both $T_{\rm eff}$ and $\log g$ (run 2) were optimized. The results are tabulated in Table 4 and compared to the observed spectra in Fig. 4.

We also tested the inclusion of the light factor as a fitted parameter (using the separated but not renormalized spectrum) with encouraging results (run 3 and run 4 in Table 4). This suggests that it is possible to reliably estimate $T_{\rm eff}$s using disentangled spectra for SB2 systems which are not eclipsing (so do not have well-determined light contributions from their component stars through

Table 4. Results of optimized genetic algorithm fitting of the hydrogen Balmer lines of star A. In the second column, the parameter which was optimized is indicated; parameters were otherwise fixed to $\log g = 3.131$ (and $\ell_{\rm A} = 1$ for the renormalized spectrum). The light-curve analysis gave $\ell_{\rm A} = 0.9394$. For comparison, analysis of the silicon ionization balance gives $T_{\rm eff\ A} = 21\,750 \pm 220$ K. In the last column, we give the difference between the values obtained in optimized fitting to the value adopted in this work. χ^2 is also given.

Run	Parameter	Hβ	Hγ	Hδ	Mean	Difference
1	$T_{\rm eff}$	21 960 ± 85	22 270 ± 70	21 860 ± 55	22 030 ± 210	280
	χ^2	0.0037144	0.0036232	0.0038175	–	
2	$T_{\rm eff}$	21 850 ± 55	21 690 ± 31	21 800 ± 45	21 780 ± 80	30
	$\log g$	3.121 ± 0.034	3.125 ± 0.031	3.123 ± 0.030	3.123 ± 0.030	0.008
	χ^2	0.0025443	0.0023554	0.0027782	–	
3	$T_{\rm eff}$	21 830 ± 70	21 620 ± 80	21 970 ± 75	21 764 ± 43	14
	ℓ	0.9541 ± 0.0021	0.9471 ± 0.0034	0.9487 ± 0.0029	0.9512 ± 0.0015	0.0118
	χ^2	0.0019254	0.0018643	0.0020095	–	
4	$T_{\rm eff}$	21 920 ± 95	21 890 ± 90	21 845 ± 95	21 885 ± 54	135
	$\log g$	3.122 ± 0.005	3.129 ± 0.007	3.139 ± 0.004	3.136 ± 0.003	0.005
	ℓ	0.9677 ± 0.0026	0.9501 ± 0.0041	0.9675 ± 0.0031	0.9643 ± 0.0018	0.0249
	χ^2	0.0015442	0.0015135	0.0016024	–	

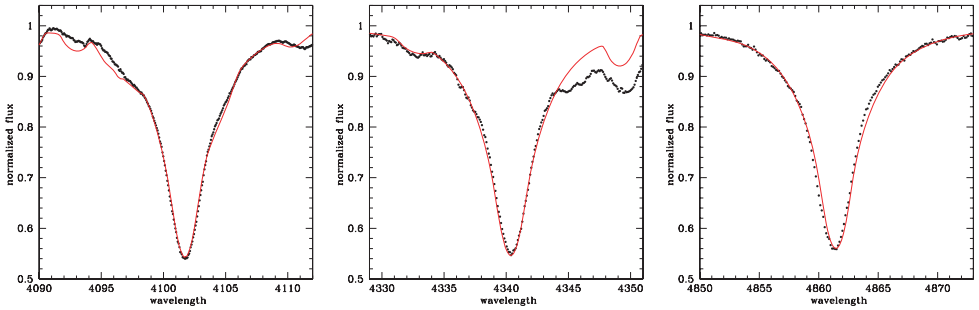

Figure 4. Comparison between the disentangled spectra (points) best-fitting theoretical spectra (solid lines) for Hδ (left-hand column), Hγ (middle panel) and Hβ (right-hand column).

eclipse analysis), which is a very interesting possibility. The results also corroborate the light contributions found in Section 5.

The two methods agree reasonably well on the value of $T_{\rm eff\ A}$, although the difference is slightly larger than 1σ for run 1. Possible sources of systematic error include the placement of the continuum for the EW measurements (particularly for the weak Si II λ λ4218 and 4231 lines), blending between Si II λ4231 and O II λ4233, and undulations in the continuum in the region of the (wide) Balmer lines. Systematic errors could also arise from the adopted atomic data (both in the statistical equilibrium calculations and in the spectral synthesis) and from the LTE assumptions of spatial homogenity, plane parallel geometry, radiative and hydrostatic equilibrium, etc. However, a study of B-type supergiants by Trundle et al. (2004), using sophisticated non-LTE analyses, yielded $T_{\rm eff}$ measurements in good agreement with the calibration of Dufton et al. (2000), which uses assumptions similar to those listed above. Despite this and the generally good agreement we find between the $T_{\rm eff}$s obtained in different ways, we have to be cautious as it is difficult to quantify the size of the systematic errors. We note that the high precision of our $T_{\rm eff}$ values comes partly from having accurate and precise $\log g$ values for the two stars. As the final we adopted $T_{\rm eff\ A} = 21\,750 \pm 280$ K where error also accounts for the determination of $T_{\rm eff}$ from hydrogen line profiles.

6.2 Microturbulence and projected rotational velocity

We have estimated the microturbulence velocity, $v_{\rm turb}$, by requiring that the measured abundance of a chemical element does not depend on the strength of its lines: the slope of a plot of EW versus abundance should be zero. The O II lines are the most numerous in the spectrum of star A, allowing us to use 32 lines for measuring $v_{\rm turb}$. We find $v_{\rm turb} = 14 \pm 1\,{\rm km\,s^{-1}}$, which is relatively high but not unusual for evolved stars with $\log g \sim 3$ (Morel et al. 2006; Hunter et al. 2007). It is encouraging that G2000 derived $v_{\rm turb} = 12 \pm 1\,{\rm km\,s^{-1}}$ using a completely different approach.

The difficulty of determining $v_{\rm turb}$ has been discussed recently by Hunter et al. (2008). For B stars, the rich spectrum of the O II ion is often used for this purpose. Uncertainties can arise between different multiplets due to the errors in the adopted atomic data or in the strength of non-LTE effects, so using a single O II multiplet is best. Dufton et al. (2005) preferred the Si III λ4560 triplet, and this approach was adopted by Hunter et al. (2008) in a large VLT-FLAMES survey of B stars. We have also tried this approach, and found almost the same value, $v_{\rm turb} = 13 \pm 1\,{\rm km\,s^{-1}}$, as above. The use of an alternative oxygen multiplet at 4072, 4076 and 4079 Å was less successful as the λ4079 line is weak and so made very shallow by rotational broadening. Therefore, an error in $v_{\rm turb}$ of $\pm 2\,{\rm km\,s^{-1}}$ would be more realistic.

Table 5. Helium abundances determined for V380 Cyg A from the set of He I lines, adopting $v_{\rm turb} = 14\,{\rm km\,s^{-1}}$ as found from the O II lines. The third column gives the helium abundances derived by Lyubimkov et al. (1996).

Line (Å)	ϵ(He) This work	ϵ(He) LRR96
4026.2	0.075 ± 0.003	–
4387.9	0.069 ± 0.005	0.123
4437.6	0.075 ± 0.005	–
4471.5	0.099 ± 0.007	0.153
4713.2	0.071 ± 0.008	0.212
4921.9	0.078 ± 0.007	0.145
5015.7	0.089 ± 0.012	(0.286)
5047.7	0.081 ± 0.008	–
5875.7	0.141 ± 0.013	(≥ 0.5)
6678.1	0.157 ± 0.018	(≥ 0.5)
mean	0.094 ± 0.031	0.158 ± 0.038

The projected rotational velocities ($v \sin i$) of the components of V380 Cyg were derived from the widths of several clean spectral features: C II λ4267, Si III λ4552, Si III λ4567, O II λ4591, O II λ4596 and O II λ4662; and avoiding He I and Mg II lines (Hensberge et al. 2000). We compared the observed line profiles to a set of theoretical spectra calculated for different $v \sin i$ values. We find $v_{\rm A} \sin i = 98 \pm 2\,{\rm km\,s^{-1}}$. The small errorbar is due to the very good agreement between the observed and calculated line profiles, and also the very high S/N (about 1000) in the disentangled spectrum of star A.

6.3 Helium abundance

V380 Cyg A has been classified as the spectral type B2 III, in agreement with the $T_{\rm eff}$ and $\log g$ we find here. In B2 stars lines of neutral helium are very strong, while lines of ionized helium are completely absent. Therefore, we calculated profiles of He I lines using the non-LTE codes DETAIL and SURFACE (see Paper I for details), for helium abundances ϵ(He) = 0.05–0.25 in steps of 0.05. The synthetic spectra were broadened by $v \sin i = 98\,{\rm km\,s^{-1}}$ and $v_{\rm turb} = 14\,{\rm km\,s^{-1}}$, and ϵ(He) was determined by χ^2 minimization to the disentangled and renormalized spectrum. The results for 10 He I lines are given in Table 5. The lines of He I at λλ4009.3 and 4120.8 were not used: our model atom does not include the first line and the second is severely blended with O II λ4121.1. The resulting mean value for the helium abundance in the photosphere of star A is $\epsilon({\rm He}) = 0.094 \pm 0.031$, which is slightly above the solar value [$\epsilon({\rm He})_\odot = 0.089$; Grevesse, Asplund & Sauval 2007]. The helium

abundances found from different He I lines span a range of 0.07–0.16 (from subsolar to 80 per cent above solar abundance) and such a large spread needs explaining.

First, the λλ4471 and 4922 line calculations are more precise as they include transitions up to the $n = 4$ level (Przybilla & Butler 2001). LRL04 discuss this in detail, and also show that the other two diffuse He I lines (λλ4026 and 4388) give a systematically lower helium abundance. LRL04 selected the λλ4471 and 4922 lines as their principal helium abundance indicators for B stars. For V380 Cyg A the mean helium abundance (by number of atoms) is $N(\mathrm{He}) = 0.072 \pm 0.006$ from λλ4026 and 4388 whereas we find $N(\mathrm{He}) = 0.089 \pm 0.010$ (equalling the solar value) from λλ4471 and 4922. This corroborates the findings by LRL04.

Secondly, the varying sensitivity of He I lines to v_{turb} might cause abundance discrepancies. In this work, we found v_{turb} from O II lines, which are the most numerous lines in the spectrum of star A. The recent literature contains some discussion about whether the v_{turb} derived from helium lines should equal that found from metallic lines such as O II, N II and Si III (see Hunter et al. 2007 and references therein). LRL04 found that v_{turb} derived from helium lines is systematically larger than that derived from metallic lines. Contrary to this, during our work on V453 Cyg (Paper I), we simultaneously fitted the helium line profiles for abundance and v_{turb}, finding a high ϵ(He) and a v_{turb} substantially lower than those from O II lines. We rejected this possibility and instead fixed v_{turb} to the 14 km s^{-1} measured from the O II lines, which resulted in a normal helium abundance.

The other lines listed in Table 5 (λλ 4713, 5016, 5048, 5876 and 6678) are known to have substantial dependences on v_{turb}. Moreover, the last two lines are unusually broad when comparing to other helium lines (Fig. 5) which indicates that other (non-thermal) broadening mechanisms are present. V380 Cyg A has evolved to the giant stage, and one could expect differences in the atmospheric velocity field compared to dwarf stars. LRL04 have discussed the possibility that asphericity and/or mass loss high in the atmospheres of hot B giants could cause excess broadening for some helium lines (Herrero, Puls & Villamariz 2000). Moreover, they have estimated that the λλ5875 and 6678 lines would give the largest helium abundances, in agreement with our findings. We will discuss this further in Section 8.

Thirdly, it is possible that the atmosphere of star A is stratified in helium. Catanzaro (2008) has argued that variations in helium abundance derived from different lines can be explained by helium stratification. A comparison of his results (for the B2 V star HD 32123) with ours (Table 5) reveals the same trends from line to line. However, a more detailed investigation of this phenomenon will require state-of-the-art non-LTE model atmospheres.

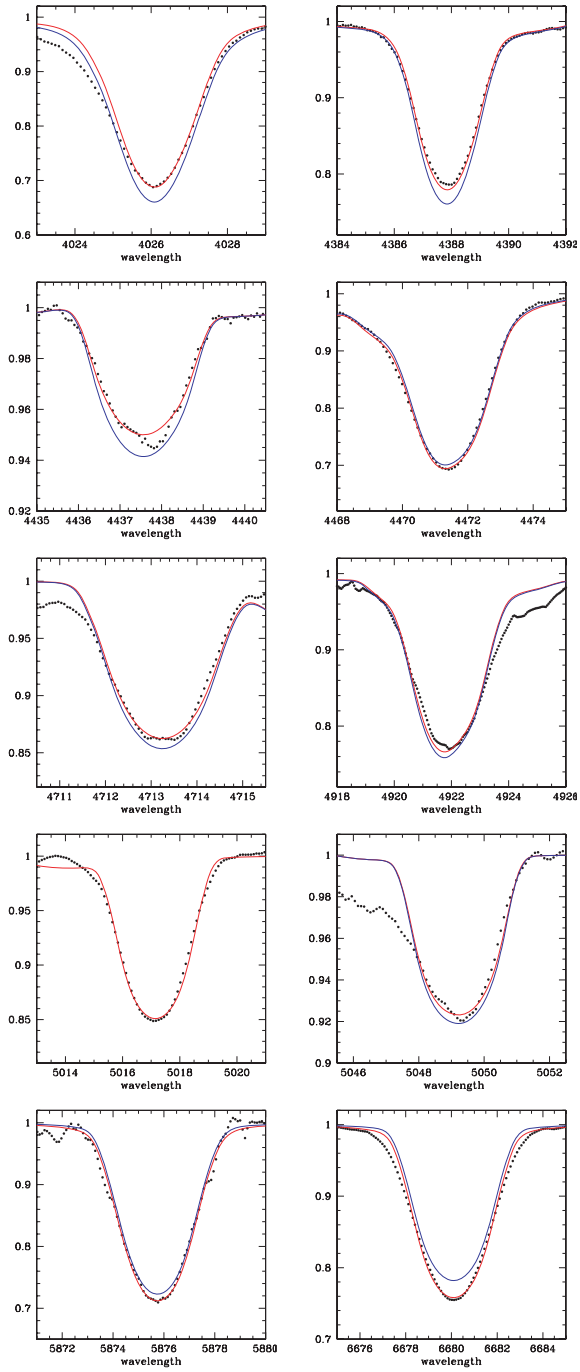

Figure 5. Profiles of a range of He I lines. Disentangled spectra are represented by the points, and theoretical line profiles which are the best fit to the disentangled profiles are shown with red lines. For comparison, profiles calculated for the solar helium abundance are also plotted with blue lines. The derived abundances are given in Table 5.

6.4 CNO abundance

The surface abundances of helium and the CNO elements are important observational results for comparison with theoretical predictions because models including rotational effects predict an enrichment of He and N and a depletion of C and O during the evolution of B stars. The optical spectra of these objects are rich in O and N lines, but have fewer C lines. We determined v_{turb} and the oxygen abundance in Section 6.2, by fitting synthetic spectra to the observed disentangled spectra of star A. Using the same approach for C and N gives results which show relatively low scatter between lines. The model carbon atom we used cannot reproduce the strongest line (C II λ4267), but the abundance estimates for the fairly strong doublet on the red wing of Hα (λλ6556 and 6559) are consistent with the abundances from other C lines.

In the spectral range 4635–4655 Å there is a bunch of relatively strong O II, C II and N II lines, which can provide reliable estimates and check on the derived abundances for these elements (PH05). In Fig. 6, we show that there is good agreement between the disentangled spectrum of star A and a theoretical spectrum calculated for the abundances derived from unblended lines (Table 6).

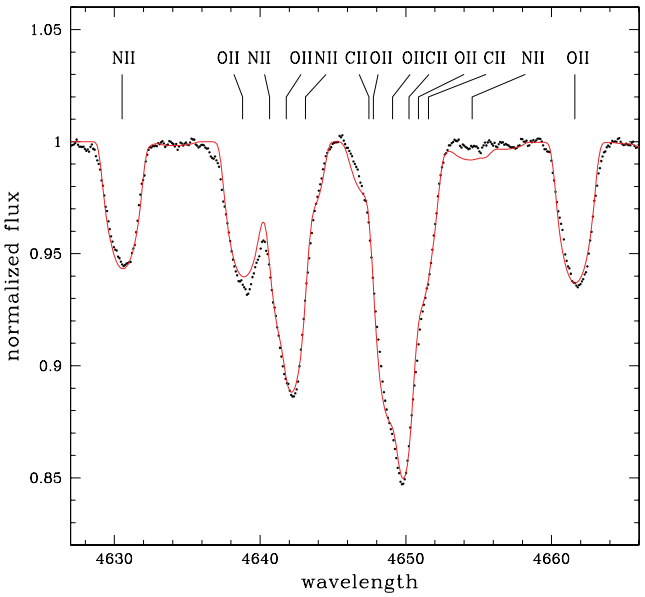

Figure 6. Comparison between the observed spectrum of star A (points) and the best-fitting synthetic spectrum (red line) calculated for the abundances listed in Table 6. The spectral range is 4625–4675 Å, which contains heavily blended lines from C II, N II and O II.

Table 6. Abundances derived for V380 Cyg A. The number of lines used is given in the brackets. Abundances for the solar photosphere and for Galactic OB stars (Hunter et al. 2009) are given in Column 3, and Column 4 lists solar abundances from Grevesse et al. (2007). Abundances for the metallic elements are given on the scale in which $N(\mathrm{He}) = 12$.

Element	Abundance	OB stars	Solar
N(He)/N(H)	0.098 ± 0.010 [10]	0.098 ± 0.014^a	0.093 ± 0.002
$\log\epsilon$(C)	8.21 ± 0.03 [8]	8.00 ± 0.19	8.39 ± 0.05
$\log\epsilon$(N)	7.52 ± 0.10 [24]	7.62 ± 0.12	7.78 ± 0.06
$\log\epsilon$(O)	8.54 ± 0.14 [35]	8.63 ± 0.16	8.66 ± 0.05
$\log\epsilon$(Mg)	7.52 ± 0.05 [1]	7.25 ± 0.17	7.53 ± 0.09
$\log\epsilon$(Si)	7.26 ± 0.18 [13]	7.42 ± 0.07	7.51 ± 0.04
$\log\epsilon$(Al)	6.04 ± 0.03 [4]	5.94 ± 0.14^b	6.37 ± 0.04

a Derived for unevolved B stars by LRL04.
b Derived for B stars with $T_{\rm eff} \leq 30\,000$ K by Daflon et al. (2003).

N is more sensitive to changes in abundances than C, for which only minute changes are predicted. However, a large spread in N abundances has been found for MS B stars, and mechanisms other than rotational mixing may be responsible (Morel et al. 2006; Hunter et al. 2009). This is highlighted by the [N/C] ratio, which is a robust indicator of CNO-processed material dredged up to the stellar surface. Its distribution in B stars is clearly bimodal (Morel 2009), with one subgroup around the solar value ($[\mathrm{N/C}]_\odot \sim -0.6$ dex) and one with significantly higher values ($[\mathrm{N/C}] \sim -0.1$ dex). With $[\mathrm{N/C}]_\mathrm{A} = -0.68 \pm 0.10$ dex, V380 Cyg A is close to the solar value. This is also true for the [N/O] ratio ($[\mathrm{N/O}]_\mathrm{A} = -1.01 \pm 0.17$ dex and $[\mathrm{N/O}]_\odot = -0.90$ dex).

6.5 Magnesium, silicon and aluminium

Determination of the abundances of metals like Mg, Si and Al makes possible an estimate of the bulk metallicity of B stars. These elements do not participate in the CNO cycle so their abundances are not affected by MS evolution. In particular, Mg is an excellent metallicity indicator because its solar and meteoritic abundances are known with high accuracy.

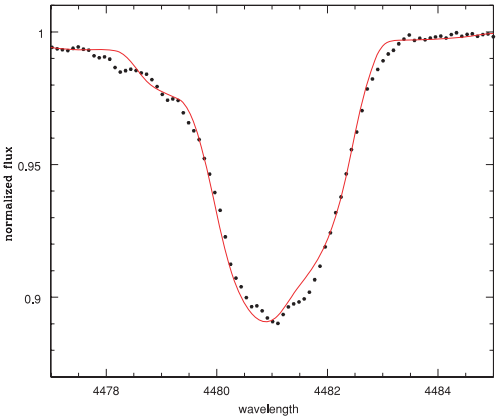

Figure 7. The best-fitting calculated profiles (solid line) of Mg II λ4481.2, which is blended with the much weaker Al III λ4479.9 line, compared to the observed profiles (filled symbols) for star A.

A disadvantage in the use of Mg for metallicity estimates in B stars is that there is only one suitable spectral line in the whole optical region: Mg II λ4481.2; although this is one of the strongest lines in the spectra of early-type stars. For stars with moderate and high $v \sin i$, an analysis of this line is complicated by blending with the neighbouring Al III λ 4479.9 line. In the $T_{\rm eff}$ range of interest here, the Al III λ4479.9 line reaches its maximum strength, and the ratio of the Al III and Mg II line EWs reaches a maximum (see Lyubimkov et al. 2005).

We derived the Al abundance for star A from three lines (λλ4512, 4671, 5766), finding a very good agreement. We used this measurement in calculating the Mg abundance from the Al III and Mg II blend at 4481 Å. We find $\log\epsilon(\mathrm{Mg}) = 7.52 \pm 0.05$, which translates to a metallicity index of $[\mathrm{Mg/H}] = -0.02 \pm 0.05$. Fig. 7 shows the fit of the synthetic spectrum to the data for this spectral line blend.

G2000 found a subsolar metallicity for star A ($[\mathrm{M/H}] = -0.44 \pm 0.07$) by fitting the system's spectral energy distribution. Elemental abundances in the present work are derived from non-LTE line profile calculations, while G2000 used the theoretical spectra generated in the LTE approximation. This might explain the disagreement between the two results.

6.6 Secondary star

Despite its faintness and small contribution to the total flux of the system, our application of SPD readily revealed the spectrum of star B (Fig. 1). Its light contribution, determined from the light-curve analysis (Section 5), is 6.1 per cent in B and 5.9 per cent in V. To renormalize its disentangled spectrum to a continuum level of unity, we have multiplied it by 16.4 and 16.9, respectively. With typically 55 spectra available for disentangling for a given spectral range, with average S/N ∼ 150, the reconstructed spectrum of star B has S/N ∼ 45. This is enough to check its $T_{\rm eff}$, but too low for a detailed abundance study.

Theoretical spectra were synthesised with $T_{\rm eff} = 19\,000$–$25\,000$ K and $\log g = 4.112$. Only strong He I lines, Mg II λ4481 and the Si III λλ4550–4580 triplet were considered in the χ^2 minimization. The mean value from eight spectral lines gives $T_{\rm eff\,B} = 21\,600 \pm 550$ K, which is consistent within the uncertainties with $T_{\rm eff\ B}$ and the $T_{\rm eff}$ ratio inferred from the light-curve analysis.

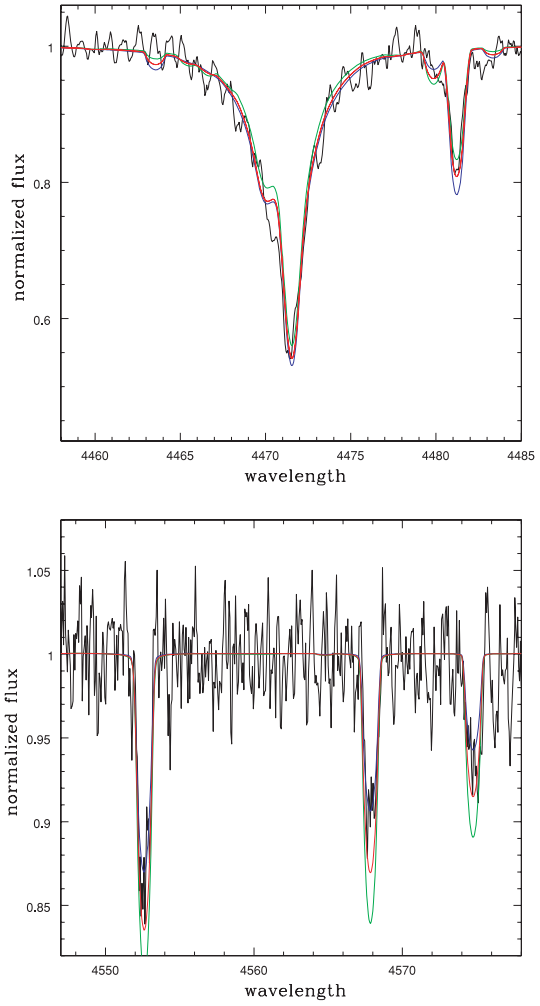

Figure 8. Comparison of the disentangled renormalized spectrum of star B to theoretical spectra for two wavelength intervals, covering He I λ4471 and Mg II λ4481 and the Si III triplet at λλ4550–4580. The synthetic spectra were calculated for $T_{\rm eff} = 20\,000$ K (blue lines), 22 000 K (red) and 24 000 K (green). Elemental abundances were the same as for star A. The low S/N of the disentangled spectrum is due to relative faintness of star B.

In Fig. 8, we compare the disentangled spectrum of star B to theoretical spectra for two wavelength intervals, covering He I λ4471 and Mg II λ4481 and the Si III triplet. The synthetic spectra were generated using the He, Mg and Si abundances found for star A. Further progress would require a substantial increase in the S/N, and thus extensive new observations.

7 THE PHYSICAL PROPERTIES OF V380 CYG

Armed with the velocity amplitudes determined in Section 4 and the results of the light-curve analysis from Section 5, we can determine the physical properties of the component stars of V380 Cyg (Table 7). For this, we use the JKTABSDIM code (Southworth, Maxted & Smalley 2005), which propagates the uncertainties on the input quantities via a perturbation analysis. The resulting error budget is dominated by the photometric parameters, highlighting the importance of obtaining a new light curve for this difficult object. Even without this, the masses and radii of the component stars are now known to accuracies of 2 per cent or better so are good enough for detailed tests of stellar evolution theory. We also find that V380 Cyg has not attained either orbital circularization or rotational synchronization.

Table 7. The absolute dimensions and related quantities determined for V380 Cyg. $V_{\rm eq}$ and $V_{\rm synch}$ are the observed equatorial and calculated synchronous rotational velocities, respectively. We adopt $\rm L_\odot = 3.826 \times 10^{26}$ W and $M_{\rm bol,\odot} = 4.75$.

	Star A	Star B
Semimajor axis ($\rm R_\odot$)	62.17 ± 0.32	
Mass ($\rm M_\odot$)	13.13 ± 0.24	7.779 ± 0.095
Radius ($\rm R_\odot$)	16.22 ± 0.26	4.060 ± 0.084
$\log g$ (cm s^{-2})	3.136 ± 0.014	4.112 ± 0.017
Effective temperature (K)	$21\,750 \pm 280$	$21\,600 \pm 550$
$\log (L/L_\odot)$	4.73 ± 0.028	3.51 ± 0.040
$M_{\rm bol}$ (mag)	-7.06 ± 0.06	-4.03 ± 0.10
$V_{\rm eq}$ (km s^{-1})	98 ± 2	43 ± 4
$V_{\rm synch}$ (km s^{-1})	66.1 ± 1.1	16.54 ± 0.34
Extinction E_{B-V} (mag)	0.20 ± 0.03	
Distance using Flower V-band BCs (pc)		1015 ± 56
Distance using Bessell V-band BCs (pc)		1034 ± 50
Distance using Bessell K-band BCs (pc)		1004 ± 23
Distance using Girardi V-band BCs (pc)		1035 ± 50
Distance using Girardi K-band BCs (pc)		1004 ± 23

With the $T_{\rm eff}$s determined above, we have found the distance to V380 Cyg via the bolometric correction (BC) method. Empirical BCs were obtained from Flower (1996), and theoretical ones from Bessell, Castelli & Plez (1998) and Girardi et al. (2002). We adopted *BV* magnitudes from the Tycho catalogue (Høg et al. 1997) and *JHK* magnitudes from Two-Micron All-Sky Survey (Skrutskie et al. 2006). There is a good agreement between different sources of BCs (Table 7). Using the Girardi et al. (2002) BCs, which are available for a wide range of passbands, we find that a reddening of $E_{B-V} = 0.20 \pm 0.03$ is needed to obtain consistent distances at optical and infrared wavelengths. For our final value, we adopt a distance of 1004 ± 23 pc from *K*-band BCs. This is in good agreement with, but more precise than, the value of 1000 ± 40 pc found by G2000.

8 PROBING THE MODELS

The two components of V380 Cyg have very different masses and radii, and thus evolutionary stages, so are a very good test of theoretical stellar models. The accuracies of the mass and radius measurements are generally 2 per cent, limited by the quality of the available light curves and the faintness of the secondary star in our spectra. A comparison with models is helped by our abundance analysis. Of particular interest is the effect of rotation on the evolution of massive stars, for which predictions are now available from Heger, Langer & Woosley (2000), Heger & Langer (2000) and Meynet & Maeder (2000). These authors found that it makes a star of a given mass more luminous and longer lived. The models also predict changes in the surface chemical composition in the sense that He and N become enriched whilst C and O are depleted. These changes are stronger for higher masses and/or initial rotational velocities.

To our knowledge, the only study which compares rotational evolutionary models with empirical data on high-mass stars in close binaries is that of Hilditch (2004). There is a known discrepancy between masses inferred from the location in the HR diagram relative to the model evolution tracks, and dynamically determined masses (Herrero et al. 1992). Hilditch found that the discrepancy did not disappear when rotating stellar models were used. We begin our comparison against V380 Cyg with the models of Schaller et al.

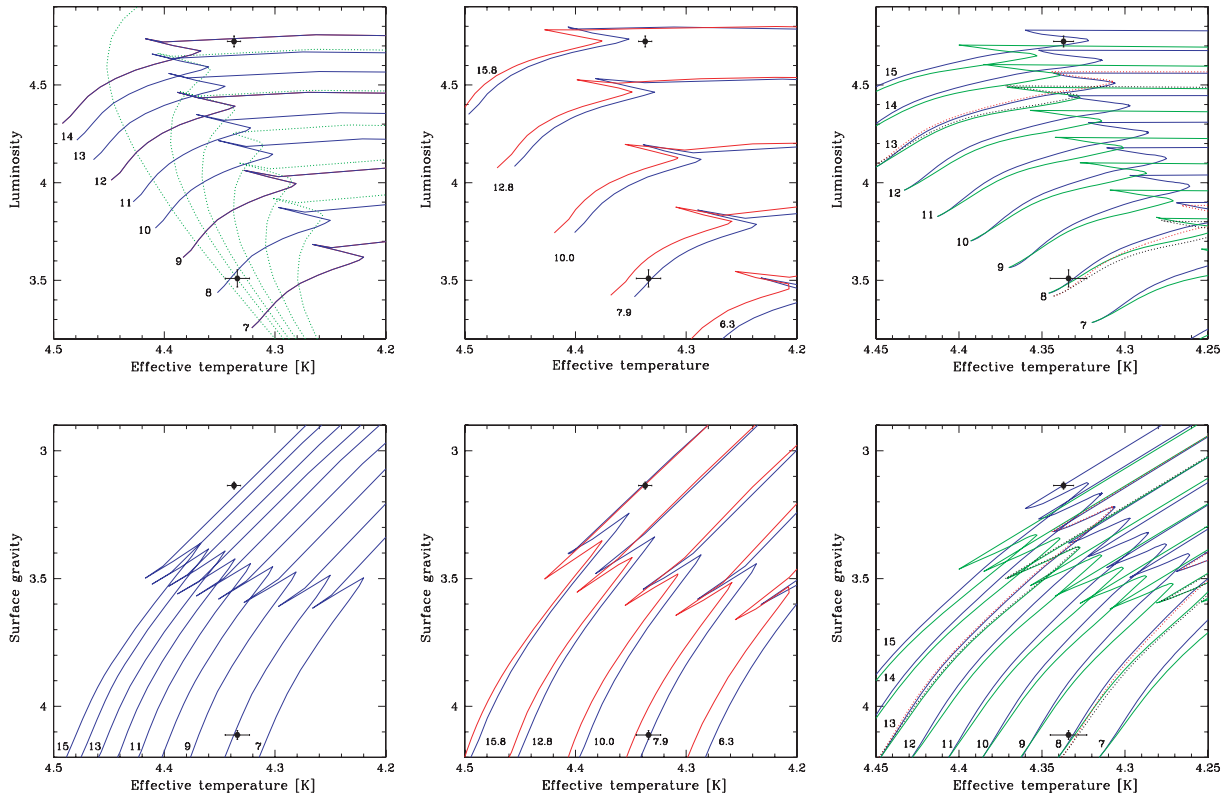

Figure 9. Comparison between stellar models and the absolute parameters of V380 Cyg in the log $T_{\rm eff}$–log L and log $T_{\rm eff}$–log g diagrams. Numbers in the plots give the masses (in $M_\odot$) for the theoretical model tracks, and the positions of the components of V380 Cyg are indicated with filled circles. Left-hand panels: models calculated with core overshooting but no rotational mixing (Schaller et al. 1992). Centre panels: models calculated by Claret (1995) for metallicity $Z = 0.02$ (blue lines) and Claret & Giménez (1995) for $Z = 0.01$ (red lines), with core overshooting but no rotational mixing. Right-hand panels: models which include rotational mixing (Ekström et al. 2008), with $\Omega/\Omega_{\rm crit} = 0.10$ (green lines), $\Omega/\Omega_{\rm crit} = 0.50$ (blue lines). Dotted red and black lines denote model predictions for the masses of V380 Cyg (13.1 and 7.8 $M_\odot$) for the same two rotational velocities.

(1992) and Claret (1995) for solar metallicity ($Z = 0.02$), moderate overshooting ($\alpha_{\rm ov} = 0.2$) and no rotational effects. Both good and bad agreements are seen for the Schaller models (Fig. 9, left-hand panels): star A is overluminous for its mass, whereas the predictions for star B perfectly match its position. From the isochrones (green dotted lines), we estimate the age of the stars to be $\tau = 9.5 \pm 0.5$ Myr. A similar situation occurs for the Claret models (Fig. 9, centre panels) for a metal abundance of $Z = 0.02$, whilst the models for $Z = 0.01$ fail to match both stars. In the $T_{\rm eff}$–log g diagram, the situation is the same: the models can match star B but strongly disagree with the properties of star A.

Fig. 9 (right-hand panels) compares evolutionary models including rotational effects with the observed properties of V380 Cyg. We interpolated in the tables published by Geneva group[4] (Ekström et al. 2008). The models are parametrized by the ratio of the rotational velocity to the critical velocity, $\Omega/\Omega_{\rm crit}$. The models for $\Omega/\Omega_{\rm crit} = 0.1$ (green tracks), and 0.5 (blue tracks) both fail to match the luminosity of star A. The discrepancy amounts to about 1.5 $M_\odot$. Star B is also slightly above the evolutionary tracks for its mass (dotted lines), but agrees within the errorbars. The $T_{\rm eff}$–log g diagram reveals the same story. It is interesting to note that in rotational evolution models the position of star A is around a critical evolutionary stage. Since rotational mixing extends the MS lifetime of high-mass stars, depending on initial rotational velocity, star A is either in the hydrogen-shell-burning phase or just at the 'blue hook' at the TAMS.

Further insight into V380 Cyg's evolution comes from its photospheric chemical composition. We interpolated in the Ekström et al. (2008) tables to the mass of star A. For $\Omega/\Omega_{\rm crit} = 0.10$ ($V_{\rm ini} \sim 40\,{\rm km\,s^{-1}}$), the increase in the photospheric helium abundance at the end of core H-burning is 0.5 per cent, whilst N/C = 0.69 and N/O = 0.24. Increasing to $\Omega/\Omega_{\rm crit} = 0.30$ gives a helium enhancement of 6 per cent, and a further increase in N at the expense of C and O (N/C = 1.12 and N/O = 0.40). Our analysis of the helium abundance in star A's photosphere (Section 6.3) gives a solar value, and we concluded that no enrichment is observed. Also, abundances of CNO elements (Section 6.4) give N/C = 0.25 and N/O = 0.11 which is exactly the initial (ZAMS) values for the models. The photospheric chemical composition appears to be untouched even though the star has reached the end of the core H-burning phase. Models for $\Omega/\Omega_{\rm crit} = 0.10$, 0.30 and 0.50 at TAMS would have rotational velocities of about 20, 80 and 160 km s^{-1}, respectively. Since star A's rotational velocity is now $\sim$100 km s^{-1}, we interpolated in the tables to find that at the TAMS a 13.13 $M_\odot$ model predicts N/C $\sim$ 0.40 and N/O $\sim$ 0.14, while initial values for this model are $({\rm N/C})_{\rm ini} \sim 0.30$ and $({\rm N/O})_{\rm ini} \sim 0.11$. The later ratio is exactly what we found for star A, whilst no changes are observed in N/C ratio. We conclude that no changes in the abundances of the CNO elements were detected, which is contrary to model predictions.

Why might this be? The evolution of stars in close binaries can be modified by several effects. In particular, tides affect their rotational

[4] http://obswww.unige.ch/Recherche/evol/

velocities and so the efficiency of rotational mixing. This has been studied theoretically using detailed calculations by De Mink et al. (2009), but unfortunately only for masses larger than V380 Cyg A. De Mink et al. found large N enhancements for the shortest period binaries, for which rotational velocities are the highest, and for high-mass primary stars which are close to filling their Roche lobes. But, for the relatively long orbital period of V380 Cyg, 12.4 d, surface abundance changes would be small (and probably too small for us to have detected). We hope that future models will extend to the parameter space occupied by V380 Cyg, allowing a direct comparison between observation and theory.

9 SUMMARY

We have presented a study of the eccentric eclipsing and double-lined spectroscopic binary V380 Cyg. The system is particularly interesting because it contains an evolved star which is at the TAMS, so is ideal for probing theoretical evolution models which include rotationally induced mixing.

New high-resolution and high-S/N spectra were secured at several telescopes, and a spectral disentangling technique was applied to obtain the individual spectra of the components, and to (simultaneously) derive the spectroscopic orbit. Although the secondary star contributes only a very small fraction of the system light (6 per cent), we were able to attain a much higher precision than previously achieved. Coupled with a re-analysis of the existing light curves of this system, we have determined the masses and radii of the two stars to accuracies of 1–2 per cent. The light ratios found in the light-curve analysis also allowed the disentangled component spectra to be accurately renormalized to the continuum level. These spectra were used to derive the effective temperatures of the two stars using two independent methods, helped by the accurate surface gravity values obtained from their known masses and radii.

The spectrum of V380 Cyg is dominated by the primary star, and its disentangled spectrum has a S/N approaching 1000 pixel^{-1} and a wavelength coverage of 3900–7000 Å. We performed a detailed abundance analysis by fitting non-LTE spectra to the observed line profiles. We found no abundance excesses for helium or metallic species, and in fact the abundances are those of a typical B star. The helium abundance analysis showed a broad range of values from different lines, which we attribute to the failure of the calculations for the lines formed higher in the photosphere due to the asphericity of the star. This problem deserves to be investigated further. It also remains possible that helium stratification might be the cause.

We have compared the bulk properties of V380 Cyg to theoretical calculations from stellar models both with and without rotational effects. No set of models fully satisfies the observations, as the primary is always overluminous for its measured mass. We are still faced with the well-known discrepancy between masses inferred from evolutionary models and those which have been dynamically measured. The mass discrepancy amounts to about 1.5 $M_\odot$ for models including rotational evolution, and about 2.5 $M_\odot$ for models which include only core overshooting, even though we have revised the mass of V380 Cyg A upwards by a substantial amount. The surface chemical composition of high-mass stars should be an important probe of theoretical models. Recent model calculations which account for rotationally induced mixing predict changes in the abundances of elements involved in the CNO cycle in high-mass stars: helium and nitrogen should be enriched and carbon and oxygen depleted (strongly depending on the mass and initial rotational velocity). For a 13 $M_\odot$ star, all available models predicted changes at the end of core hydrogen burning, but the abundance pattern we derived in this work resembles with that of a star at the ZAMS. We can conclude only that a detailed analysis performed for V380 Cyg A does not corroborate theoretical predictions of the chemical evolution of high-mass stars. We are currently engaged in extending the sample of close binaries for which such comparisons can be made.

ACKNOWLEDGMENTS

Based on the observations collected at the Centro Astronómico Hispano Alemán (CAHA) at Calar Alto, operated jointly by the Max-Planck Institut für Astronomie and the Instituto de Astrofísica de Andaluca (CSIC), and on observations made with the NOT, operated on the island of La Palma jointly by Denmark, Finland, Iceland, Norway and Sweden, in the Spanish Observatorio del Roque de los Muchachos of the Instituto de Astrofisica de Canarias. We would like to thank several colleagues for obtaining spectra of V380 Cyg at the 2-m telescope in Ondřejov: M. Šlechta, J. Polster, M. Ceniga, M. Netolický, P. Škoda, V. Votruba, P. Hadrava, D. Korčáková, J. Libich, K. Uytterhoeven, B. Kučerová and J. Kubát. We acknowledge a constructive and timely response from our reviewer Prof Philip Dufton. This work was funded through a research grant to KP from Croatian Ministery of Science and Education. JS acknowledges financial support from STFC in the form of grant number ST/F002599/1. This work was partly funded from a research grant to PK from ESA PECS project No. 98058.

REFERENCES

Andersen J., 1991, A&AR, 3, 91
Batten A. H., 1962, Publ. Dom. Astrophys. Obs. Victoria, 12, 91
Becker S., Butler K., 1990, A&A, 235, 326
Bessell M., Castelli F., Plez B., 1998, A&A, 333, 231
Butler K., 1984, PhD thesis, Univ. London
Catanzaro G., 2008, MNRAS, 385, L33
Claret A., 1995, A&AS, 109, 441
Claret A., 1998, A&AS, 131, 395
Claret A., 2000, A&A, 363, 1081
Claret A., 2001, MNRAS, 327, 989
Claret A., 2003, A&A, 399, 1115
Claret A., 2007, A&A, 475, 1019
Claret A., Giménez A., 1995, A&AS, 114, 549
Daflon S., Cunha K., Smith V. V., Butler K., 2003, A&A, 399, 525
De Mink S. E., Cantiello M., Langer N., Pols O. R., Brott I., Yoon S.-Ch., 2009, A&A, 497, 243
Dufton P. L., McErlean N. D., Lennon D. J., Ryans R. S. I., 2000, A&A, 353, 311
Dufton P. L., Ryans R. S. I., Trundle C., Lennon D. J., Hubeny I., Lanz T., Allende Prieto C., 2005, A&A, 434, 1125
Ekström S., Meynet G., Maeder A., Barblan F., 2008, A&A, 478, 467
Evans C. J. et al., 2005, A&A, 437, 467
Evans C. J. J. K., Lennon D. J., Smartt S. J., Trundle C., 2006, A&A, 456, 623
Flower P. J., 1996, ApJ, 469, 355
Frandsen S., Lindberg B., 1999, in Harttunen H., Piirola V., eds, Astrophysics with the NOT. Univ. Turku, Turku, p. 71
Giddings J., 1981, PhD thesis, Univ. London
Gies D. R., Lambert D. L., 1992, ApJ, 387, 673
Girardi L., Bertelli G., Bressan A., Chiosi C., Groenewegen M. A. T., Marigo P., Salasnich B., Weiss A., 2002, A&A, 391, 195
Grevesse N., Asplund M., Sauval A. J., 2007, Space Sci. Rev., 130, 105
Guinan E. F., Ribas I., Fitzpatrick E. L., Giménez Á., Jordi C., McCook G. P., Popper D. M., 2000, ApJ, 544, 409 (G2000)

Hadrava P., 1995, A&AS, 114, 393
Heger A., Langer N., 2000, ApJ, 544, 1016
Heger A., Langer N., Woosley S. E., 2000, ApJ, 528, 368
Hensberge H., Pavlovski K., 2007, in Hartkopf W. I., Guinan E. F., Harmanec P., eds, IAU Symp. 240, Binary Stars as Critical Tools and Tests in Contemporary Astrophysics. Cambridge Univ. Press, Cambridge, p. 136
Hensberge H., Pavlovski K., Verschueren W., 2000, A&A, 358, 553
Hensberge H., Ilijić S., Torres K. B. V., 2008, A&A, 482, 1031
Herrero A., Kudritzki R. P., Vilchez J. M., Kunze D., Butler K., Haser S., 1992, A&A, 261, 209
Herrero A., Puls J., Villamariz M. R., 2000, A&A, 354, 193
Hilditch R. W., 2004, in Hilditch R. W., Hensberge H., Pavlovski K., eds, ASP Conf. Ser. Vol. 318, Spectroscopically and Spatially Resolving the Components of the Close Binary Systems. Astron. Soc. Pac., San Francisco, p. 198
Hill G., Batten A. H., 1984, A&A, 141, 39
Høg E. et al., 1997, A&A, 323, L57
Horn J., Kubat J., Harmanec P., Koubský P., Hadrova P., Šimon V., Stefe V., Skoda P., 1996, A&A, 309, 521
Huang W., Gies D. R., 2006, ApJ, 648, 591
Hunter I. et al., 2007, A&A, 466, 277
Hunter I. et al., 2008, ApJ, 676, L29
Hunter I. et al., 2009, A&A, 496, 841
Hynes R. I., Maxted P. F. L., 1998, A&A, 331, 167
Ilijić S., Hensberge H., Pavlovski K., Freyhammer L. M., 2004, in Hilditch R. W., Hensberge H., Pavlovski K., eds, ASP Conf. Ser. Vol. 318, Spectroscopically and Spatially Resolving the Components of Close Binary Systems. Astron. Soc. Pac., San Francisco, p. 111
Kurucz R. L., 1979, ApJS, 40, 1
Kurucz R. L., 1993, CD-ROM 13, SAO
Langer N., Cantiello M., Yoon S.-C., Hunter I., Brott I., Lennon D., de Mink S., Verheijdt M., 2008, in Bresolin F., Crowther P. A., Puls J., eds, IAU Symp. 250, Massive stars as cosmic engines. Cambridge Univ. Press, Cambridge, p. 167
Leushin V. V., 1988, SvA, 32, 517
Leushin V. V., Topilskaya G. P., 1986, Astrophysics, 25, 503
Lyubimkov L. S., 1998, Astron. Rep., 42, 52
Lyubimkov L. S., Rachkovskaya T. M., Rostophchin S. I., Tarasov A. E., 1996, Astron. Rep., 40, 46
Lyubimkov L. S., Rostopchin S. I., Lambert D. L., 2004, MNRAS, 351, 745 (LRL04)
Lyubimkov L. S., Rostopchin S. I., Rachkovskaya T. M., Poklad D. B., Lambert D. L., 2005, MNRAS, 358, 193
Maeder A., Meynet G., 2000, ARA&A, 38, 143
Meynet G., Maeder A., 2000, A&A, 361, 101
Morel T., 2009, Commun. Asteroseis., 158, 122
Morel T., Butler K., Aerts C., Neiner C., Briquet M., 2006, A&A, 457, 651
Nieva M. F., Przybilla N., 2007, A&A, 467, 295
Pavlovski K., 2004, in Hilditch R. W., Hensberge H., Pavlovski K., eds, ASP Conf. Ser. Vol. 318, Spectroscopically and Spatially Resolving the Components of Close Binary Systems. Astron. Soc. Pac., San Francisco, p. 206
Pavlovski K., Hensberge H., 2005, A&A, 439, 309 (PH05)
Pavlovski K., Southworth J., 2009, MNRAS, 394, 1519 (Paper I)
Pfeiffer M. J., Frank C., Baumüller D., Fuhrmann K., Gehren T., 1998, A&AS, 130, 381
Popper D. M., Guinan E. F., 1998, PASP, 110, 572
Press W. H., Teukolsky S. A., Vetterling W. T., Flannery B. P., 1992, Numerical Recipes in Fortran 77: The Art of Scientific Computing, Cambridge Univ. Press, Cambridge
Przybilla N., Butler K., 2001, A&A, 379, 955
Schaller G., Schaerer D., Meynet G., Maeder A., 1992, A&AS, 96, 269
Simon K. P., Sturm E., 1994, A&A, 281, 286
Škoda P., 1996, in Jakoby G. H., Barnes J., eds, ASP Conf. Ser. Vol. 101, Astronomical Data Analysis Software and Systems V. Astron. Soc. Pac., San Francisco, p. 187
Skrutskie M. F. et al., 2006, AJ, 131, 1163
Southworth J., 2008, MNRAS, 386, 1644
Southworth J., Clausen J. V., 2007, A&A, 461, 1077
Southworth J., Maxted P. F. L., Smalley B., 2004, MNRAS, 351, 1277
Southworth J., Maxted P. F. L., Smalley B., 2005, A&A, 429, 645
Southworth J., Bruntt H., Buzasi D. L., 2007, A&A, 467, 1215
Southworth J. et al., 2009, MNRAS, in press (arXiv:0907.3356)
Tamajo E., Pavlovski K., Southworth J., 2009, A&A, submitted
Trundle C., Lennon D. J., Puls J., Dufton P. L., 2004, A&A, 417, 217
Trundle C., Dufton P. L., Hunter I., Evans C. J., Lennon D. J., Smartt S. J., Ryans R. S. I., 2007, A&A, 471, 625
Van Hamme W., 1993, AJ, 106, 2096
Wilson R. E., 1979, ApJ, 234, 1054
Wilson R. E., 1993, in Leung K. C., Nha I. S., eds, ASP Conf. Ser. Vol. 38, New Frontiers in Interacting Binary Star Research. Astron. Soc Pac., San Francisco, p. 91
Wilson R. E., 1990, ApJ, 356, 613
Wilson R. E., Devinney E. J., 1971, ApJ, 166, 605
Wilson R. E., Van Hamme W., 2004, Computing Binary Star Observables. Univ. Florida, Gainesville

APPENDIX A: OBSERVING LOGS FOR THE DATA PRESENTED IN THIS WORK

The tables in this section contain observing logs for each of the fours sets of spectroscopic observations used in this work. In each case, the orbital phases have been calculated with ephemeris derived by G2000.

Table A1. Observing log for the Ondřejov red spectra of V380 Cyg.

Set	ID	HJD	Phase	S/N
AUO	nh060033	53224.5345	963.1629	406
AUO	nj050015	53284.3204	967.9744	476
AUO	nj110016	53290.3615	968.4607	523
AUO	of190036	53541.4822	988.6701	256
AUO	pi240037	54003.3681	1025.8419	327
AUO	pj100025	54019.4183	1027.1337	302
AUO	pj160020	54025.3728	1027.6128	315
AUO	pj170017	54026.2822	1027.6860	329
AUO	pj200028	54029.3709	1027.9347	363
AUO	qd020024	54193.5319	1041.1460	433
AUO	qd040052	54195.5864	1041.3114	240
AUO	qd110012	54202.6237	1041.8779	282
AUO	qd130029	54204.4341	1042.0234	234
AUO	qd140035	54205.4133	1042.1023	329
AUO	qd150023	54206.4880	1042.1888	302
AUO	qd160023	54207.5143	1042.2715	320
AUO	qd190051	54210.5260	1042.5138	306
AUO	qd200076	54211.5794	1042.5984	154
AUO	qd220035	54213.4753	1042.7512	147
AUO	qd220036	54213.4893	1042.7522	424
AUO	qd230013	54214.4278	1042.8279	377
AUO	qd250015	54216.5346	1042.9973	645
AUO	qd300010	54221.3884	1043.3878	365
AUO	qe010020	54221.5111	1043.3978	153
AUO	qe030013	54224.3838	1043.6289	472
AUO	qe170014	54238.4871	1044.7640	185
AUO	qf230025	54275.5113	1047.7437	231
AUO	qg140028	54296.5112	1049.4337	268
AUO	qg140030	54296.5256	1049.4349	304
AUO	qg170012	54299.3604	1049.6628	371
AUO	qg260022	54308.5021	1050.3988	342
AUO	qh050031	54318.4729	1051.2010	313
AUO	qh130008	54326.3361	1051.8339	191
AUO	qh130010	54326.3563	1051.8354	396
AUO	qh170015	54330.4312	1052.1633	180

Table A2. Observing log for the Ondřejov blue spectra of V380 Cyg.

Set	ID	HJD	Phase	λ_c (Å)	S/N
AUO	ni170011	53266.3564	966.5286	4500	231
AUO	ni180017	53267.3871	966.6116	4500	379
AUO	nj050010	53284.2734	967.9706	4500	269
AUO	nj100002	53289.2876	968.3742	4200	95
AUO	nj120017	53291.2617	968.5330	4500	67
AUO	nj240036	53303.4095	969.5107	4500	253
AUO	nj250003	53304.2597	969.5789	4500	304
AUO	nk250003	53335.2304	972.0715	4500	264
AUO	oe260012	53517.4736	986.7380	4350	224
AUO	pj160016	54025.3308	1027.6096	4900	139
AUO	qd160028	54207.5544	1042.2747	4900	213
AUO	qd190080	54210.5981	1042.5195	4900	83
AUO	qd220060	54213.5538	1042.7574	4900	210
AUO	qd270032	54218.5272	1043.1577	4900	254
AUO	qd280024	54219.4498	1043.2318	4900	187
AUO	qd290038	54220.5512	1043.3206	4900	176
AUO	qe030018	54224.4380	1043.6333	4900	191
AUO	qe180020	54239.4456	1044.8411	4350	129
AUO	qf090021	54261.5286	1046.6183	4440	150
AUO	qf110020	54263.4758	1046.7751	4400	122
AUO	qf160017	54268.3798	1047.1697	4400	76
AUO	qg140025	54296.4497	1049.4287	4400	198
AUO	qg160015	54298.5406	1049.5969	4400	148
AUO	qh050018	54318.3959	1051.1948	4400	148

Table A3. Observing log for the Victoria red spectra of V380 Cyg.

Set	ID	HJD	Phase	S/N
DAO	3c05618	54232.9356	1044.3172	306
DAO	3c07248	54259.9013	1046.4873	287
DAO	3c07992	54274.8548	1047.6907	248
DAO	3c08291	54276.9189	1047.8569	48
DAO	3c12337	54340.7187	1052.9914	236

Table A4. Observing log of the NOT and CAHA spectra of V380 Cyg.

Set	ID	HJD	Phase	S/N
NOT		54039.37711	1028.7399	166
NOT		54039.38248	1028.7403	309
NOT		54039.39750	1028.7416	242
CAHA	A167	54607.46305	1074.4586	56
CAHA	A168	54607.46750	1074.4590	146
CAHA	A181	54607.61685	1074.4709	156
CAHA	A182	54607.62454	1074.4716	176
CAHA	A190	54607.67179	1074.4753	144
CAHA	A191	54607.67839	1074.4760	130
CAHA	B161	54608.63799	1074.5530	116
CAHA	B162	54608.64601	1074.5536	136
CAHA	B164	54608.66251	1074.5552	80
CAHA	B165	54608.67026	1074.5558	164
CAHA	C181	54609.55296	1074.6268	32
CAHA	C182	54609.56075	1074.6274	20
CAHA	D158	54610.52706	1074.7052	144
CAHA	D159	54610.53474	1074.7058	148
CAHA	H200	54691.47874	1081.2201	66
CAHA	H201	54691.48664	1081.2207	54
CAHA	H202	54691.49426	1081.2213	60
CAHA	H220	54691.67199	1081.2355	42
CAHA	H221	54691.67967	1081.2361	36
CAHA	H222	54691.68733	1081.2368	36
CAHA	I191	54692.33182	1081.2887	60
CAHA	I192	54692.33942	1081.2893	64
CAHA	I219	54692.60461	1081.3107	70
CAHA	I220	54692.61226	1081.3113	70
CAHA	I221	54692.61994	1081.3119	84
CAHA	J215	54693.61367	1081.3917	124
CAHA	J216	54693.62132	1081.3923	120
CAHA	J217	54693.62911	1081.3931	72
CAHA	K189	54694.31946	1081.4486	156
CAHA	K190	54694.32706	1081.4493	152
CAHA	K221	54694.59423	1081.4707	96
CAHA	K222	54694.59957	1081.4709	130
CAHA	K223	54694.60717	1081.4716	118
CAHA	M184	54696.32683	1081.6102	232
CAHA	M208	54696.53837	1081.6272	144
CAHA	M209	54696.54484	1081.6276	126
CAHA	M210	54696.55136	1081.6282	120
CAHA	M217	54696.58198	1081.6306	154
CAHA	M218	54696.58974	1081.6313	144
CAHA	M219	54696.59739	1081.6328	108

This paper has been typeset from a TEX/LATEX file prepared by the author.